Interannual and Interdecadal Variabilities of Spring Rainfall over Northeast China and Their Associated Sea Surface Temperature Anomaly Forcings

Article *in* Journal of Climate · November 2019

DOI: 10.1175/JCLI-D-19-0302.1

CITATIONS
2

READS
227

4 authors, including:

Lu Rui
Nanjing University of Information Science & Technology
4 PUBLICATIONS **5** CITATIONS
SEE PROFILE

Zhiwei Zhu
Nanjing University of Information Science & Technology
42 PUBLICATIONS **611** CITATIONS
SEE PROFILE

Tim Li
University of Hawai'i System
385 PUBLICATIONS **14,498** CITATIONS
SEE PROFILE

Interannual and Interdecadal Variabilities of Spring Rainfall over Northeast China and Their Associated Sea Surface Temperature Anomaly Forcings

RUI LU

Key Laboratory of Meteorological Disaster, Ministry of Education/Joint International Research Laboratory of Climate and Environment Change/Collaborative Innovation Center on Forecast and Evaluation of Meteorological Disasters, Nanjing University of Information Science and Technology, Nanjing, and Yichun Meteorological Bureau, Heilongjiang, China

ZHIWEI ZHU

Key Laboratory of Meteorological Disaster, Ministry of Education/Joint International Research Laboratory of Climate and Environment Change/Collaborative Innovation Center on Forecast and Evaluation of Meteorological Disasters, Nanjing University of Information Science and Technology, Nanjing, China

TIM LI

Key Laboratory of Meteorological Disaster, Ministry of Education/Joint International Research Laboratory of Climate and Environment Change/Collaborative Innovation Center on Forecast and Evaluation of Meteorological Disasters, Nanjing University of Information Science and Technology, Nanjing, China, and International Pacific Research Center and Department of Atmospheric Sciences, University of Hawai'i at Mānoa, Honolulu, Hawaii

HAIYANG ZHANG

Key Laboratory of Meteorological Disaster, Ministry of Education/Joint International Research Laboratory of Climate and Environment Change/Collaborative Innovation Center on Forecast and Evaluation of Meteorological Disasters, Nanjing University of Information Science and Technology, Nanjing, China

(Manuscript received 24 April 2019, in final form 14 November 2019)

ABSTRACT

An empirical orthogonal function (EOF) analysis was conducted for spring precipitation gauge data over northeast China (NEC). The first EOF mode is characterized by a homogenous rainfall pattern throughout NEC. The corresponding principal component has both significant interannual and interdecadal variations. This leading mode explains a large portion of the total NEC spring rainfall (NECSR) variances and is statistically independent from other higher modes. The physical processes responsible for the interannual and interdecadal variabilities were investigated via observational diagnoses and numerical experiments. On the interannual time scale, NECSR is mainly affected by the SST anomalies (SSTAs) in the northern tropical Atlantic Ocean. When the SSTAs are positive, the subsequently induced positive precipitation and convection can stimulate two quasi-barotropic Rossby wave trains over the mid- to high latitudes. A cyclonic anomaly center of the Rossby wave train appears over northeastern Asia, leading to a positive rainfall anomaly in the region. On the interdecadal time scale, NECSR is mainly influenced by the SSTAs over the warm-pool region. Positive SSTAs in the warm-pool region result in enhanced convection (ascending motion) around the Maritime Continent and suppressed convection (descending motion) over the central equatorial Pacific Ocean. This zonal dipole convection pattern stimulates a quasi-barotropic circulation pattern with an anticyclonic anomaly over the Tibetan Plateau and a cyclonic anomaly over northeastern Asia. The cyclonic anomaly over northeastern Asia enhances the NECSR. Numerical experiments further suggested that the convective heating anomaly over the Maritime Continent, rather than cooling over the central equatorial Pacific, plays a more essential role in driving the interdecadal rainfall variability of NECSR.

Supplemental information related to this paper is available at the Journals Online website: https://doi.org/10.1175/JCLI-D-19-0302.s1.

Corresponding author: Zhiwei Zhu, zwz@nuist.edu.cn

DOI: 10.1175/JCLI-D-19-0302.1

1. Introduction

Northeast China (NEC) has long been a large grain production base. Spring is the sowing season in NEC, and the rainfall supports agriculture and livelihood of over 120 million people. The amount of precipitation greatly affects the growth of grain seedlings during sowing, which ultimately determines the annual grain production in the region. Besides the influences on agriculture, abnormal NEC spring rainfall (NECSR) can also result in flooding or drought, leading to adverse socioeconomic impacts. Unraveling the hitherto elusive physical mechanisms of NECSR variability and further improving its prediction accuracy are of great significance to food security as well as disaster prevention and mitigation.

Previous studies on rainfall variability over NEC have mainly focused on the summer season (Zhao et al. 2018; Fang et al. 2018; Liu et al. 2011; Han et al. 2015). For instance, Sun et al. (2007) revealed that the moisture of summer rainfall in NEC comes from subtropical, South China Sea and South Asia monsoon areas. Sun et al. (2017) suggested that an anomalous cyclone tends to develop over NEC with an intensified and westward-shifted western Pacific subtropical high in summer. These factors can cause a strong East Asian summer monsoon and therefore more rainfall over NEC. Zhao and Sun (2007) and Hu et al. (2010) emphasized the importance of cutoff lows over Eurasian mid- to high latitudes in the formation of rainfall over NEC. Shen et al. (2011) indicated that the interannual variation in rainfall over NEC is first controlled by a cold vortex in early summer (May and June) and then by the East Asian summer monsoon in late summer (July and August). The large-scale circulation anomalies associated with abnormal summer rainfall over NEC are attributable to sea surface temperature anomalies (SSTAs) (Feng et al. 2006) over the southeastern Pacific Ocean (Gao and Gao 2015) and tropical Indian Ocean (Han et al. 2018b), and Arctic sea ice cover changes (Zhu et al. 1999; Singarayer et al. 2006; Jaiser et al. 2012; Li and Wang 2013; Wu et al. 2008; Wu et al. 2009).

Winter snowfall over NEC has also received extensive attention (Wang et al. 2011; Wang and He 2012). Sun and Wang (2013) suggested that the water vapor transport from eastern China and the Sea of Japan are the origins of the water vapor for widespread snowfall in NEC. Han et al. (2018a) revealed the interdecadal change of the interannual variation between the snowfall in NEC and the North Atlantic and Indian Ocean SST in the 1990s and argued that the NEC snowfall was first significantly related to the SSTAs over the tropical Indian Ocean in 1961–90, but then was related to the SSTAs over the North Atlantic Ocean in 1996–2013. Zhou et al. (2018) revealed that the frequency of snowfall events in NEC has decreased because of the reduction in light snowfall events, and the mean intensity of snowfall events has increased since the 1960s. The total amount of snow and the number of snow days in NEC are expected to decrease further by the end of the twenty-first century, based on Regional Climate Model, version 4 (RegCM4) (Giorgi et al. 2012), simulations under the $4.5\,\mathrm{W\,m^{-2}}$ representative concentration pathway (RCP4.5) scenario.

In summary, previous works on precipitation variability over NEC have mostly focused on the summer and winter seasons, with little attention having been paid to the physical processes of spring rainfall variability. In fact, the performance of numerical historical simulations of rainfall over NEC is inferior (see Fig. S1 in the online supplemental material). Motived by the lack of scientific understanding on NESRC and the imperative of accurately predicting NECSR's variability, the present study aims to unravel the underlying mechanisms of the variability and provide clue for improving its seasonal prediction.

The rest of the paper is structured as follows: section 2 describes the data and model utilized in this work. Section 3 shows the characteristics of the leading mode of NECSR. Sections 4 and 5 investigate the physical mechanisms of variabilities of NECSR on interannual and interdecadal time scales, respectively. Conclusion remarks are given in section 6.

2. Data and model

The datasets employed in this study were: 1) monthly gauge precipitation data over China gridded to a horizontal resolution of 0.25° × 0.25° (Wu and Gao 2013); 2) monthly atmospheric field datasets with a horizontal resolution of 2.5° × 2.5° from the National Centers for Environmental Prediction–National Center for Atmospheric Research Reanalysis I (Kalnay et al. 1996); 3) monthly mean SST data gridded to a 2.0° × 2.0° horizontal resolution from the improved Extended Reconstructed SST dataset, version 5 (Huang et al. 2017); and 4) global monthly precipitation data with a 2.5° × 2.5° horizontal resolution provided by the National Oceanic and Atmospheric Administration Precipitation Reconstruction (Chen et al. 2002). The time span of all datasets was from 1961 to 2012. Spring denotes the seasonal mean for March–May (MAM).

Empirical orthogonal function (EOF) analysis (Lorenz 1956) was used to extract the leading mode of NECSR. The anomalous precipitation field was selected

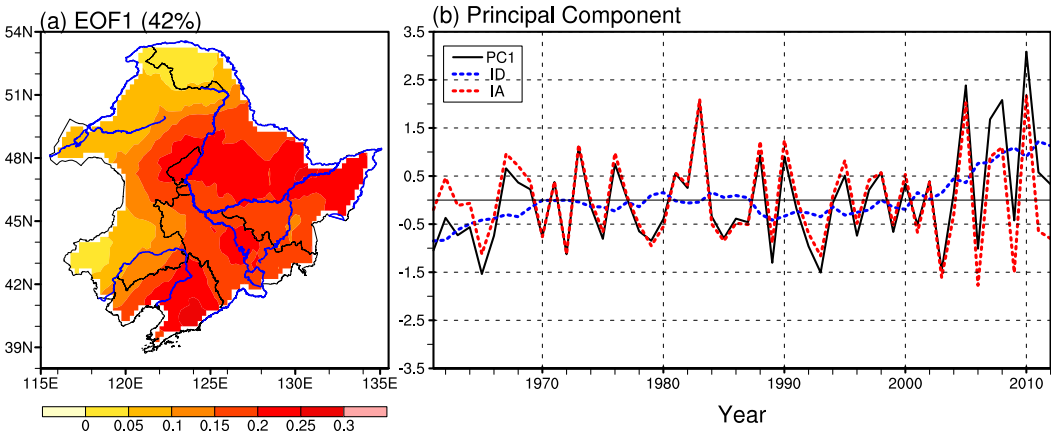

FIG. 1. The (a) spatial pattern (shading; mm day^{-1}) and (b) PC (black line) of the first EOF mode of NECSR. The blue lines in (a) represent the main rivers in the region, and the dashed red and blue lines in (b) denote the interannual and interdecadal components, respectively, of the PC (black line).

to conduct the EOF analysis. The analysis domain of NEC included the provinces of Heilongjiang, Jilin, Liaoning, and eastern Inner Mongolia, which is consistent with previous studies (e.g., Du et al. 2013; Fang et al. 2018). The interdecadal component of the principal component (PC) of the EOF mode was obtained by a 9-yr running mean of the raw PC, and the interannual component of the PC was extracted by removing the interdecadal component from the raw PC. Pearson correlation and linear regression analysis was employed to explore the relationship between meteorological fields and NECSR. The Student's t test was applied to assess the statistical significance, and the effective degrees of freedom N_{edof} is evaluated following Bretherton et al. (1999) and Wang et al. (2017):

$$N_{\text{edof}} = N(1 - r_1 r_2)/(1 + r_1 r_2),$$

where N represents the sample number and r_1 and r_2 indicate the lag-1 autocorrelations of the two time series.

To understand the origin and the atmospheric teleconnection associated with the variability of NECSR, the Rossby wave source (Sardeshmukh and Hoskins 1988) and wave activity flux (WAF) are calculated. The phase-independent WAF was calculated based on the following formula by Takaya and Nakamura (2001):

$$W = \frac{1}{2|\overline{U}|}\begin{bmatrix} \overline{u}(\psi_x'^2 - \psi'\psi_{xx}) + \overline{v}(\psi_x\psi_y' - \psi'\psi_{xy}) \\ \overline{u}(\psi_x'\psi_y' - \psi'\psi_{xy}') + \overline{v}(\psi_y'^2 - \psi'\psi_{yy}') \end{bmatrix},$$

where an overbar and a prime represent the climatological mean and anomaly, respectively; ψ and $U = (u, v)$ represent the streamfunction and the horizontal wind, respectively; and W denotes the two-dimensional Rossby WAF.

To validate the proposed mechanisms of NECSR's variability, an atmospheric general circulation model (AGCM) with the prescribed observational climatological fields was employed. This model was developed from the global spectrum dry AGCM (Held and Suarez 1994) of the Geophysical Fluid Dynamics Laboratory. It is a global spectral model that uses sigma ($\sigma = p/p_s$) as its vertical coordinate and a T42 Gaussian grid horizontal resolution. The basic equations include momentum, temperature, and the logarithm of surface pressure equations, together with a diagnostic equation for vertical velocity. An observed spring (MAM) mean state was prescribed as the model basic state, which was taken from the long-term mean (1981–2010) of reanalysis data. To investigate the atmospheric response to the rainfall diabatic heating, the atmospheric heating profile, which mimics the observation, was prescribed at different levels of the troposphere in the AGCM. This model has been widely used to investigate the formation of various atmospheric teleconnection patterns (Li 2006; Zhu and Li 2018).

3. Leading modes of NECSR

The first EOF mode of NECSR explains 42% of the total variances and is statistically significant and independent from higher modes according to North's criteria (North et al. 1982). Therefore, this study only focuses on this first EOF mode of NECSR. Figure 1a shows that the spatial pattern of the first EOF mode of NECSR is characterized by the homogeneous rainfall pattern throughout the region, with maximum positive loading over eastern NEC and a gradually decline westward. The PC of this leading mode presents significant

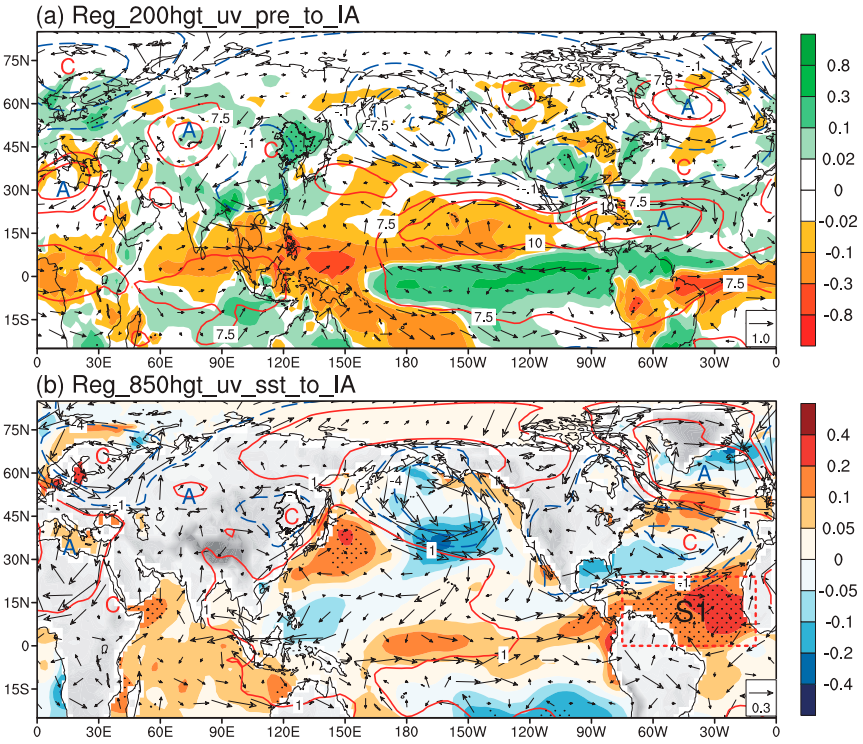

FIG. 2. Regressed (a) 200-hPa geopotential height (contours; gpm), wind (vectors; m s^{-1}), and precipitation (shading; mm day^{-1}) in spring (MAM) onto the interannual component of PC1. (b) As in (a), but for 850-hPa geopotential height (contours; gpm) and SST (shading; °C). The black solid line delineates the region of NEC; the red dash–outlined box indicates the region of S1 for calculating the ALI. The letters "A" and "C" indicate the centers of anticyclonic and cyclonic anomalies, respectively. Dotted areas are statistically significant at the 95% confidence level. The gray shading over the land in (b) represents the topography.

variabilities on both interannual and interdecadal time scales (Fig. 1b). The interannual and interdecadal component accounts for 82% and 18% of total variances of the PC, respectively. In the following sections, we separately explore the physical processes for the variabilities on these two time scales.

4. Physical process for the interannual variability of NECSR

To examine the dynamic and thermodynamic fields associated with the interannual variability of NECSR, the atmospheric circulation and SST fields are regressed onto the interannual component of PC1, as shown in Fig. 2. It can be seen in Fig. 2a that enhanced NECSR is accompanied by enhanced rainfall over the equatorial central/eastern Pacific and northern tropical Atlantic. The atmospheric fields are characterized by two quasi-barotropic Rossby wave trains over the mid- to high latitudes (Fig. 2). One barotropic Rossby wave train is characterized by five anomalous cyclones or anticyclones centered in the North Atlantic, southern tip of Greenland, northern Europe, central Asia, and northeastern Asia, respectively. The other is characterized by five anomalous cyclones or anticyclones centered in the North Atlantic, Mediterranean Sea, Red Sea, central Asia, and northeastern Asia, respectively. Note that the wave trains are similar to the circulation anomalies that associated with the interannual variability of the spring atmospheric heat source over the Tibetan Plateau (Cui et al. 2015). The barotropic cyclonic anomaly over northeastern Asia favors northward transportation of water vapor into NEC, thus, leading to enhanced NECSR.

It can be seen clearly in Fig. 2b that the precipitation anomaly over northern tropical Atlantic is closely associated with the statistically significant positive SSTA, whereas the anomalous precipitation over equatorial Pacific shows no statistically significant relation with the local SST. The positive SSTA over northern equatorial Atlantic could induce the positive precipitation anomaly which further excites Rossby wave train. Therefore, the process can be considered as the ocean affects the atmosphere. Although the equatorial Pacific shows strong rainfall anomaly signal, the underlying Pacific SSTA is

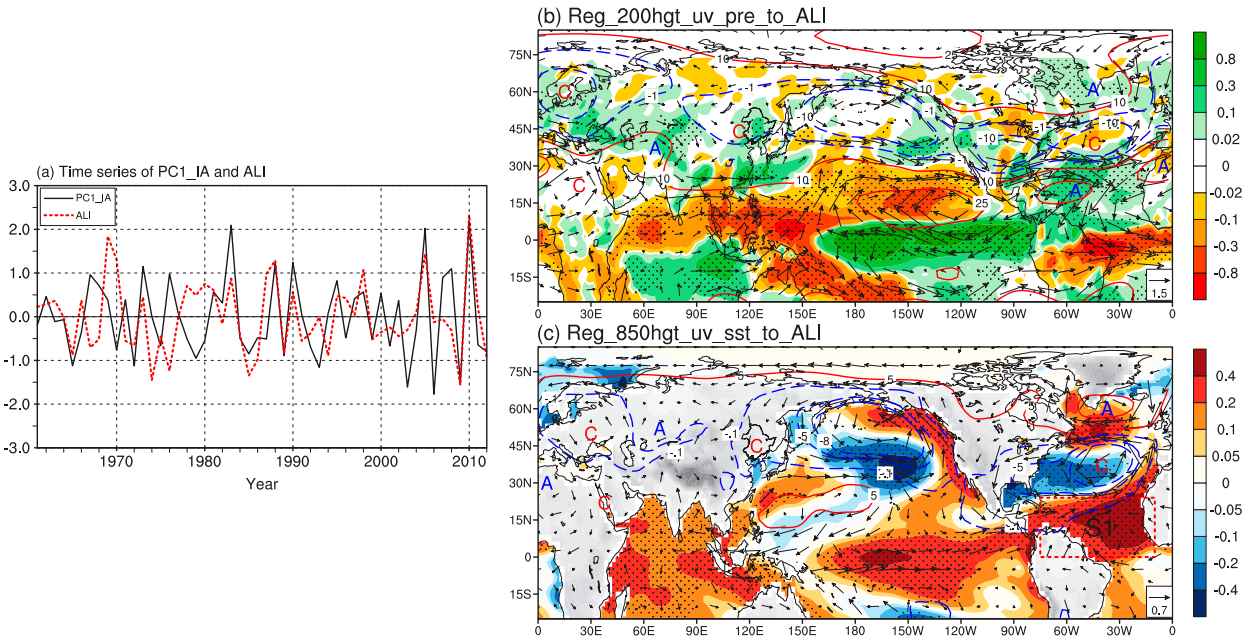

FIG. 3. (a) Time series of interannual component of PC1 and ALI. (b),(c) As in Fig. 2, but for the regression onto the ALI.

not significant, suggesting that the Pacific SSTA may not play an active role in driving the convective heating. Therefore, in this study, the enhanced precipitation anomaly associated with the positive SSTA over northern tropical Atlantic may play a more important role for inducing diabatic heating and the associated atmospheric teleconnection, although the precipitation anomaly is relatively weak in the northern tropical Atlantic when compared with that over the equatorial Pacific region.

Figure 2b also shows pronounced positive SSTA over the northwestern Pacific in the midlatitudes, which is associated with the local anticyclonic circulation (high pressure) anomaly. We may infer that the positive SSTA is caused by the cloudlessness that associated with the anticyclonic circulation (high pressure) anomaly via increasing downward solar radiation. Note that the associated local precipitation anomaly is negative or zero, suggesting that the SSTA over the northwestern Pacific in the midlatitudes may be largely driven by the atmospheric circulation anomaly (Li and Wang 2018). However, once this positive SSTA appears, it could reinforce the anticyclonic anomaly (see Fig. S2 of the online supplemental material for the dynamic model simulation) via the eddy feedback (Peng and Whitaker 1999), and the southwesterly wind over the western flank of the anomalous anticyclone could further enhance the NECSR. In the present study, we consider the positive northwestern Pacific SSTA over the midlatitudes as a passive resultant of the atmospheric forcing rather than the forcing itself, although this positive SSTA could modulate atmospheric circulation and exert an amplification effect for the interannual variability of NECSR.

Given that the northern tropical Atlantic positive SSTA accompanied by the local enhanced precipitation is more likely the forcing of the atmospheric circulation, do the northern tropical Atlantic SST anomalies indeed play a vital role in driving the mid- to high-latitude Rossby wave train and, in turn, the variability of NECSR? To check this possibility, the northern tropical Atlantic sector (S1: 0°–24°N, 75°–10°W) was selected as the key region, and an Atlantic SST index (ALI) was defined as the area-averaged SSTA over S1. The time correlation coefficient between the ALI and interannual component of PC1 reaches 0.44, exceeding the 99% confidence level (Fig. 3a). Figures 3b and 3c present the dynamic and thermodynamic fields regressed onto ALI. The northern equatorial Atlantic SST shows significant regression coefficients (Fig. 3c), which is similar to Fig. 2b. Figure 3b shows positive precipitation anomalies over the northern tropical Atlantic and NEC, which resembles that in Fig. 2a. Although the northern branch of the quasi-barotropic wave train in Figs. 3b and 3c shows much weaker amplitude and south shifted comparing to that in Fig. 2, two similar quasi-barotropic wave trains appear in the mid- to high latitudes of the Northern Hemisphere, leading to a cyclonic circulation (low pressure) anomaly over NEC.

Based on the above observational diagnosis, a mechanism is proposed that the SSTA in the northern tropical

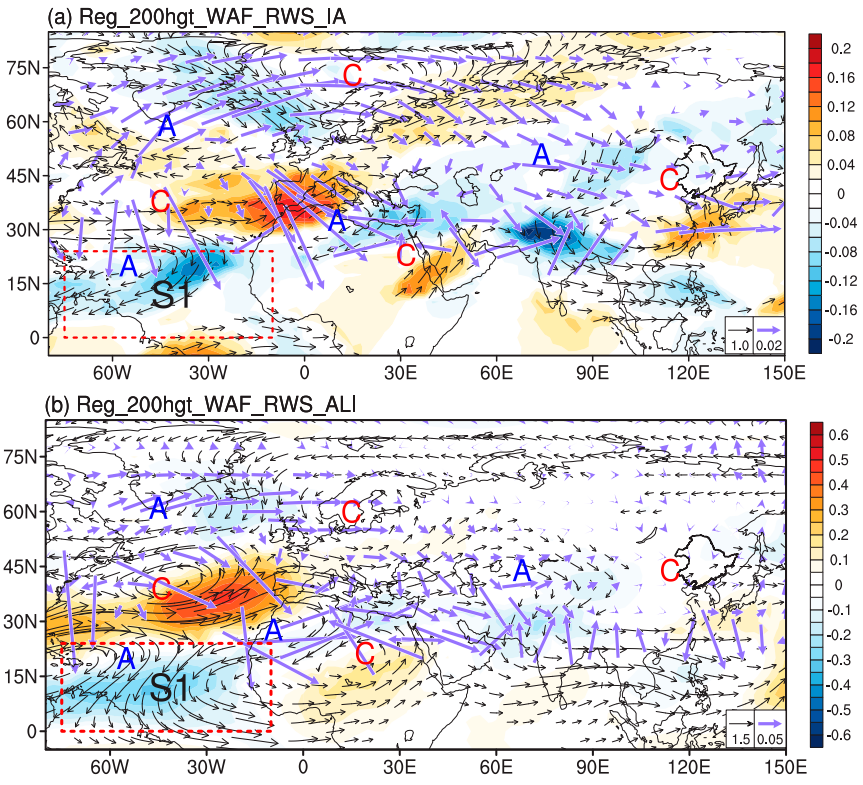

FIG. 4. Regressed spring wind (black vectors; $m\,s^{-1}$), Rossby wave source (shading; $1 \times 10^{-10}\,s^{-2}$), and WAF (blue vectors; $m^2\,s^{-2}$) at 200 hPa onto (a) the interannual component of PC1 and (b) the interannual component of ALI. The black solid line delineates the region of NEC; the red dash–outlined box indicates the region of S1 for calculating the ALI. The letter "A" and "C" indicate the centers of anticyclonic and cyclonic anomalies, respectively.

Atlantic play the key role in driving the interannual variability of NECSR via inducing two mid- to high-latitude Rossby wave trains. The northern tropical Atlantic warm SSTA induces local convection/precipitation, then, the convective heating released by the precipitation perturbs the upper-troposphere westerly jet steam, leading to two quasi-barotropic wave trains from the northern Atlantic to northeastern Asia. A cyclonic circulation anomaly dominates NEC, corresponding to the local positive precipitation anomalies.

To validate the existence of the mid- to high-latitude Rossby wave train, Fig. 4a plots the WAFs and Rossby wave source with respect to the interannual component of PC1. The Rossby wave sources are mainly located over North Atlantic and the Rossby wave energy propagates from the Atlantic to NEC, across the entire mid- to high latitudes in Eurasia. The wave energy originates from the north of S1 and propagates along two pathways to northeastern Asia: one initially travels northeastward to northern Europe and then southeastward to northeastern Asia, while another travels directly eastward to northeastern Asia. Figure 4b plots the same WAFs and Rossby wave source but with respect to the ALI. Although the northern pathway is relatively weaker with respect to ALI, it can be seen that the Rossby wave source and energy propagation are quite consistent to that in Fig. 4a, suggesting that the mid- to high-latitude Rossby wave train indeed stems from the northern tropical Atlantic.

Note that the SSTA associated with the interannual component of PC1 in Fig. 2b are significant only over the northern tropical Atlantic. This SSTA pattern is associated with more robust northern branch of the Rossby wave train as shown in Figs. 2a and 4a. However, the SSTA associated with the ALI in Fig. 3c shows a significant tripole pattern. With two additional SSTA forcings over the North Atlantic, the northern branch of the Rossby wave train become weak and shifts southward as shown in Figs. 3b and 4b relative to that in Figs. 2a and 4a. These indicate each pole of the Atlantic SSTA tripole pattern possibly exert independent or even offset impacts on the northern branch of the Rossby wave train. The specific influence of each pole of the tripole SSTA over Atlantic merits further exploration.

The Rossby wave source (RWS) over Asia that is associated with the interannual component of PC1 in Fig. 4a is missing when with respect to the ALI as shown in Fig. 4b. This may suggest that the rainfall/convection over Asia could produce a new RWS over the local region (Fig. 4a) and further induce wave activity over the downstream region (Zhu and Li 2016). On the contrary, the RWS with respect to the ALI become weak during its eastward propagation journey along the paths of the Rossby wave train.

To further confirm the proposed mechanism and the Rossby wave train, numerical experiments were conducted using the AGCM. To mimic the observational heating profile, the maximum heating rate in the model was prescribed at $\sigma = 0.5$ (approximately 500 hPa), and it was reduced to 80% at $\sigma = 0.3$, 80% at $\sigma = 0.7$, 50% at $\sigma = 0.9$, and 10% at $\sigma = 0.1$ (see Fig. S3a of the online supplemental material). Figure 5 shows the temporal evolution of the 200-hPa geopotential height and wind response to the atmospheric heating over the northern tropical Atlantic. The propagation pathways of the quasi-barotropic Rossby wave in the AGCM are basically consistent with that in Fig. 4. At the equilibrium state (integrated after about 30 days), anomalous cyclonic anomalies appear with centers over the North Atlantic, northern Europe, Red Sea, and northeastern Asia and anticyclonic anomalies appear with centers over the tropical Atlantic, southern Greenland, Mediterranean Sea, and central Asia, thus reproducing two quasi-barotropic Rossby wave trains similar to that in Fig. 2.

In summary, based on both observational diagnosis and numerical simulations, the interannual variability of NECSR stems from the northern tropical Atlantic SSTA via inducing two mid- to high-latitude Rossby wave trains. Specifically, the positive northern tropical Atlantic SSTA could induce a local positive rainfall anomaly, which releases latent heating and perturbs the westerly jet steam, forming the quasi-barotropic wave trains that enhance NECSR.

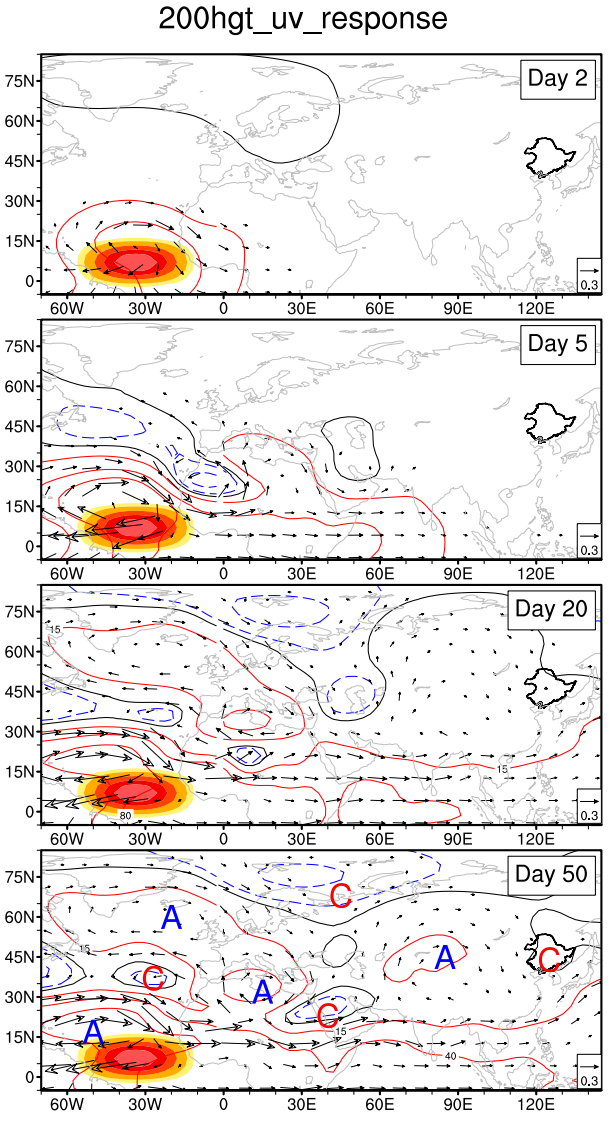

FIG. 5. The 200-hPa geopotential height (contours; gpm) and wind (vectors; m s^{-1}) response to the atmospheric heating over the northern tropical Atlantic. The red shading indicates the horizontal profile of the imposed idealized heating with the maximum amplitude at 1 K day^{-1}. The letters "A" and"C" indicate the centers of anticyclonic and cyclonic anomalies, respectively. The black solid line delineates the region of NEC.

5. Physical process for the interdecadal variation of NECSR

Having analyzed the interannual variability of NECSR, we now turn to the physical mechanism of the interdecadal variability of NECSR. To explore the associated dynamic and thermodynamic fields, the atmospheric circulation and SST fields are regressed onto the interdecadal component of PC1, as shown in Fig. 6. Figure 6a shows that enhanced NECSR is accompanied by a zonal dipole rainfall pattern over tropical region, with enhanced rainfall over the Maritime Continent and suppressed rainfall over the tropical central Pacific. The anomalous zonal dipole precipitation pattern over the tropics is mainly caused by the pronounced positive SST anomalies around the Maritime Continent. The atmospheric fields (Fig. 6) are characterized by two anomalous circulation systems, with anticyclonic anomaly center around Tibetan Plateau and cyclonic anomaly center over northeastern Asia. Does the pronounced SSTA around the warm pool play the vital role for the interdecadal variability of NECSR? To check this possibility, the circulation and SST fields associated with the

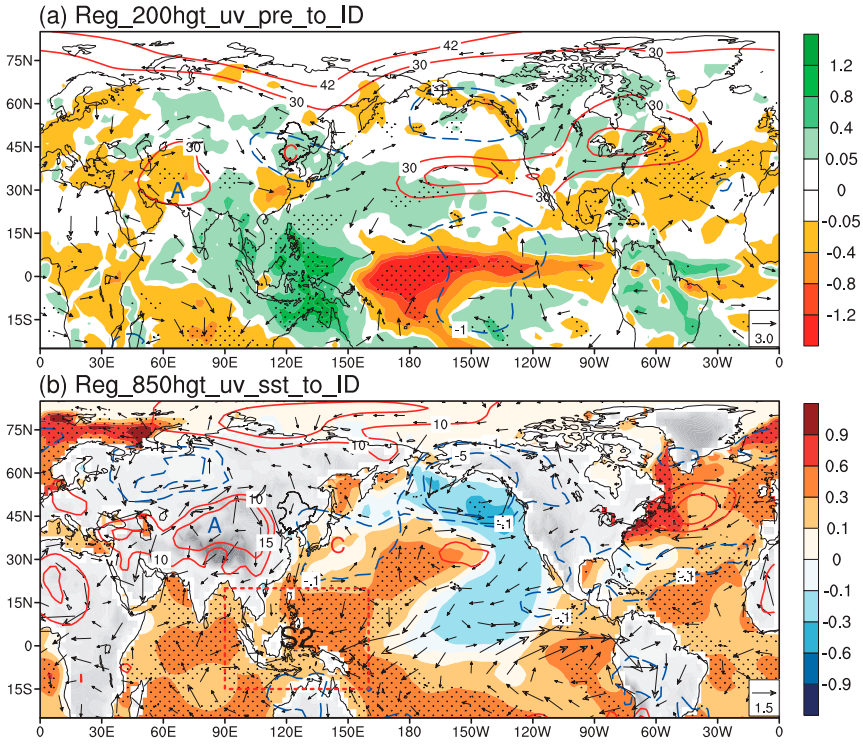

FIG. 6. As in Fig. 2, but regressed onto the interdecadal component of PC1. The black solid line delineates the region of NEC; the red dash–outlined box indicates the region of S2 for calculating the MCI.

warm-pool SSTA were examined. The area-averaged SSTA over the warm-pool sector (S2: 15°S–20°N, 90°–160°E) was defined as Maritime Continent SST index (MCI) as shown in Fig. 7a. Figures 7b and 7c present the dynamic and thermodynamic fields regressed onto MCI. Figure 7b shows positive precipitation anomalies near the Maritime Continent and negative precipitation anomalies over the central tropical Pacific, consistent

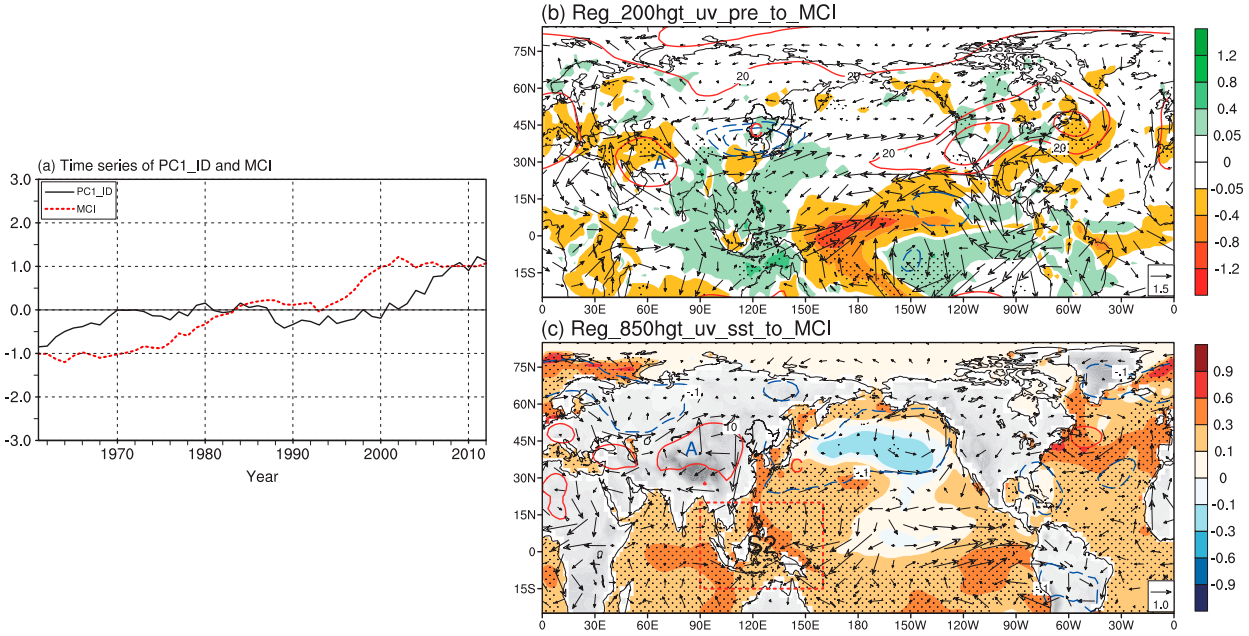

FIG. 7. (a) Time series of interdecadal component of PC1 and MCI. (b),(c) As in Fig. 2, but for the regression onto the MCI.

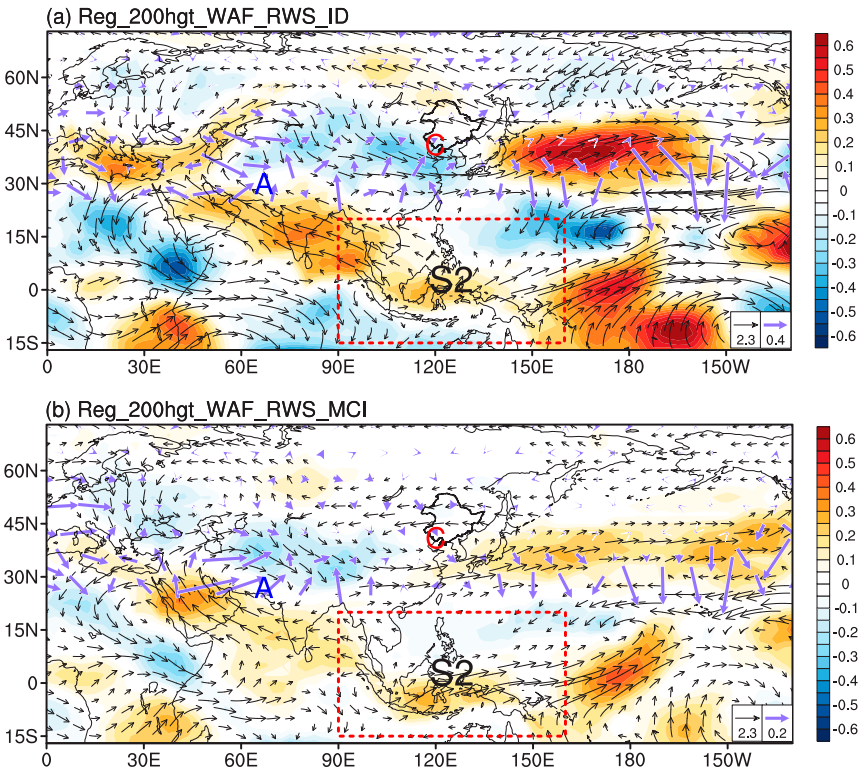

FIG. 8. Regressed spring wind (black vectors; m s^{-1}), Rossby wave source (shading; 1×10^{-10} s^{-2}), and WAF (blue vectors; m^2 s^{-2}) at 200 hPa onto (a) the interdecadal component of PC1 and (b) the interannual component of MCI. The black solid line delineates the region of NEC; the red dash–outlined box indicates the region of S2 for calculating the MCI. The letters "A" and "C" indicate the centers of anticyclonic and cyclonic anomalies, respectively.

to Fig. 6a. In the mid- to high latitudes of the Northern Hemisphere, a similar circulation anomaly pattern appears with a cyclonic circulation anomaly dominating NEC. The SST around the Maritime Continent shows significant regression coefficients (Fig. 7c), which is also quite similar to Fig. 6b.

Based on the above observational diagnosis, a physical mechanism is proposed that the SSTA over the warm pool is responsible for the interdecadal variability of NECSR via inducing a quasi-barotropic dipole circulation anomaly pattern. First, the positive SSTA around the Maritime Continent induces a zonal dipole convection/precipitation anomaly pattern, with enhanced convection/precipitation over the warm pool and suppressed convection/precipitation over the tropical central Pacific. Then, the diabatic heating released by the zonal dipole precipitation pattern over the tropics excites a quasi-barotropic dipole circulation anomaly pattern with an anticyclonic anomaly around Tibetan Plateau and a cyclonic anomaly over northeastern Asia. The cyclonic anomaly dominates NEC, corresponding to the local positive rainfall anomalies.

Whether the cyclonic anomaly over northeastern Asia is indeed induced by the heating from the tropics? Fig. 8a plots the WAFs and Rossby wave source with respect to the interdecadal component of PC1. The results indicate that the Rossby wave source and wave energy originates from the northwest side of S2 (northern Indian Ocean), and propagates from Tibetan Plateau to northeastern Asia, suggesting that tropical convection may play an important role in driving NECSR. Figure 8b plots the same WAFs and Rossby wave source but with respect to the MCI. It can be seen that the Rossby wave source and energy propagation are quite consistent to that in Fig. 8a, suggesting that the circulation anomaly pattern is driven by the SSTA over warm pool.

To further confirm the proposed mechanism, numerical simulation experiments were conducted using the AGCM with the additional prescribed atmospheric heating or cooling. This time, to mimic the observational heating profile, the maximum heating or cooling rate in the model was prescribed at $\sigma = 0.3$ (approximately 300 hPa), and it was reduced to 70% at $\sigma = 0.5$, 40% at

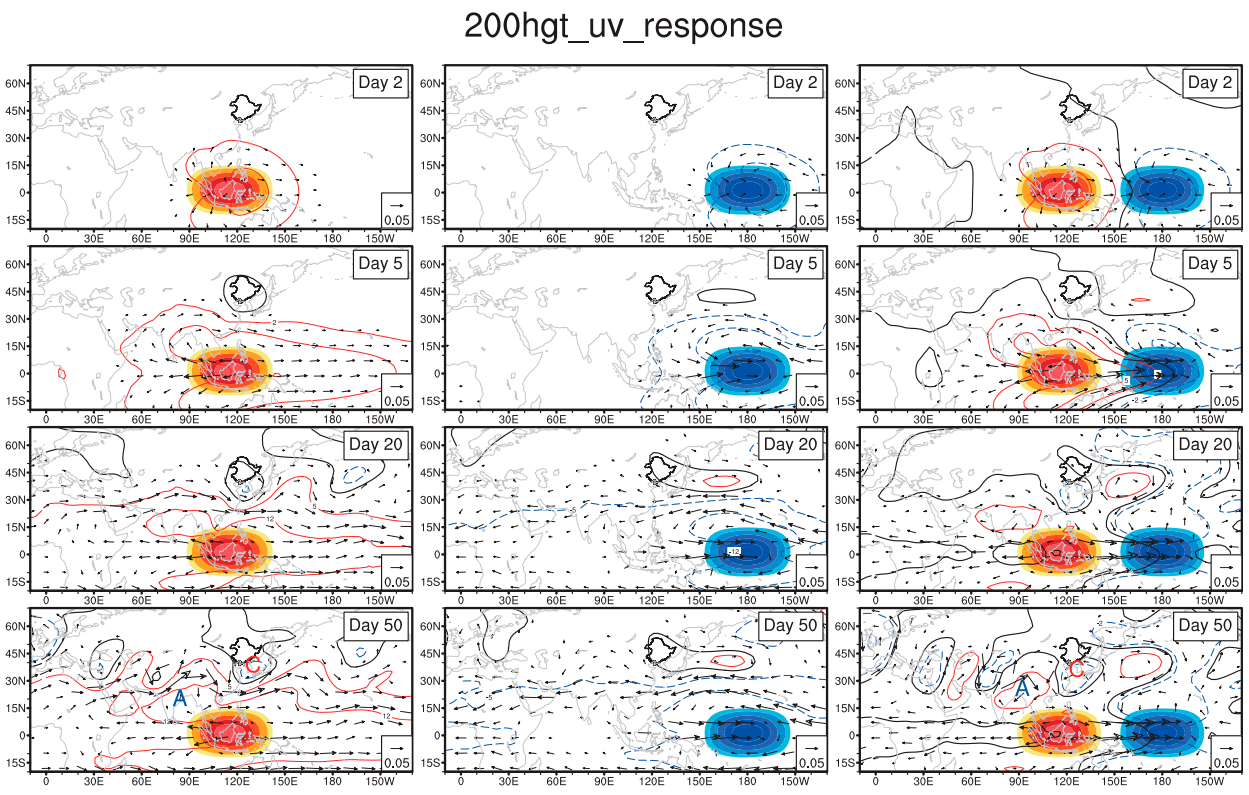

FIG. 9. As in Fig. 5, but with the red and blue shading indicating the imposed idealized heating and cooling, respectively.

$\sigma = 0.1$, 40% at $\sigma = 0.7$ and 10% at $\sigma = 0.9$ (see Fig. S3b in the online supplemental material). Since the cyclonic anomaly over northeastern Asia is associated with the SSTA-induced tropical zonal dipole convection anomaly pattern, three experiments are conducted to examine the relative importance of the two convection anomalies. As shown in Fig. 9a, if only a single heating is prescribed over the warm pool, a Gill-type atmospheric response (Gill 1980) can be induced. To the northeast of the Rossby wave response (in terms of the anticyclonic anomaly), a cyclonic anomaly appears over northeastern Asia, suggesting that the Maritime Continent heating plays a vital role in driving the cyclonic anomaly over northeastern Asia. On the contrary, when only a cooling is given in the tropical central Pacific, an anticyclonic anomaly is observed over northeastern Asia (Fig. 9b), which is opposite to that of the Maritime Continent heating. When the Maritime Continent heating and the tropical central Pacific cooling are both given, a more realistic circulation anomaly pattern is induced, with two anticyclonic anomalies over the Tibetan Plateau and midlatitude western Pacific, and a cyclonic anomaly over northeastern Asia, resembling the observation as shown in Fig. 6a. In sum, the Maritime Continent heating, rather than the central Pacific cooling, plays a more essential role in driving the interdecadal variability of NECSR.

One may ask whether the linear trend of PC1 would influence the results of the interdecadal variability of NECSR; we double checked the interdecadal variability of the PC1 and its associated meteorological fields after removing the linear trend. The result shows that the associated anomalous precipitation field of detrended interdecadal component of PC1 is very similar to that of the interdecadal component of PC1 without detrend (see Fig. S4 of the online supplemental material). The detrended associated precipitation fields also shows a dipole precipitation pattern over the tropics just like that in Fig. 6a, and the anomalous atmospheric circulation fields are also consistent. Note, however, that while the enhanced convection over the Maritime Continent kept the same, the suppressed convection (i.e., the detrended result in Fig. S4) is not significant as that in Fig. 6a (i.e., nondetrended result). The difference between the two results indeed statistically confirmed our simulations that the enhanced convection around the Maritime Continent play the primary role in driving the interdecadal variability of NECSR, while the suppressed convection over central equatorial Pacific is not essential for the interdecadal variability of NECSR.

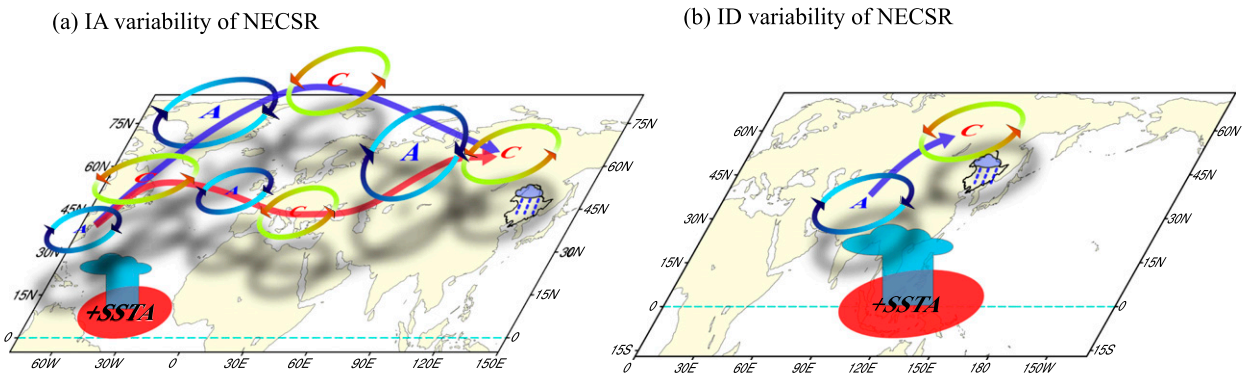

FIG. 10. The schematic diagram to illustrate the physical processes associated with the (a) interannual and (b) interdecadal variabilities of the leading mode of NECSR. The black solid line delineates the region of NEC; the red elliptical region indicates the key area of SST anomaly. The letters "A" and "C" indicate the center of anticyclonic and cyclonic anomalies, respectively, at 200 hPa.

In sum, based on observational diagnoses and numerical simulations, the interdecadal variability of NECSR stems from the SSTA around the Maritime Continent via inducing a cyclonic anomaly over northeastern Asia. Specifically, the positive SSTA around the warm-pool region can induce a positive rainfall anomaly over the Maritime Continent and a negative rainfall anomaly over the tropical central Pacific. Whereas the zonal dipole rainfall anomalies can induce a more realistic circulation pattern over the Northern Hemisphere, the Maritime Continent heating plays a more essential role in driving the cyclonic anomaly over northeastern Asia and the interdecadal variation of NECSR.

6. Conclusions

In this study, the leading mode of NECSR is obtained by an EOF analysis. The spatial pattern of the first EOF mode shows a homogeneous structure throughout the region, and its PC has both significant interannual and interdecadal variabilities.

As shown in the schematic diagram of Fig. 10a, the interannual variability of NECSR is mainly influenced by the SSTA in the northern tropical Atlantic. When the northern tropical Atlantic SSTA is positive, atmospheric diabatic heating can be excited by the SSTA-induced convection/precipitation. The diabatic heating stimulates two quasi-barotropic mid- to high-latitude Rossby wave trains from the Atlantic to northeastern Asia. As one center of the Rossby wave train, a cyclonic anomaly controls NEC, favoring northward transportation of moisture into NEC, and therefore enhanced NECSR.

As illustrated in Fig. 10b, the interdecadal variability is mainly controlled by SSTAs over the warm-pool region. The warm-pool SSTA could lead to a zonal dipole convection/precipitation anomaly pattern, with enhanced convection/precipitation over the warm pool and suppressed convection/precipitation over the tropical central Pacific. The tropical heating/cooling stimulates a quasi-barotropic circulation pattern with anticyclonic anomaly over around Tibetan Plateau and cyclonic anomaly over northeastern Asia. The cyclonic anomaly favors enhanced NECSR. Furthermore, numerical experiments suggested that Maritime Continent heating, rather than the cooling over the tropical central Pacific, plays a more important role in driving the NECSR variability.

Although a cyclonic anomaly brings enhanced NECSR on both interannual and interdecadal time scales, the difference between them is notable. The cyclonic anomaly on interannual time scale is part of the mid- to high-latitude zonal Rossby wave train. NEC is to the east of the cyclonic anomaly center and on the west side of the anticyclonic anomaly, therefore, the anomalous southwesterly wind could transport the warm and moist air from the tropical ocean to NEC, leading to enhanced NECSR. However, the cyclonic anomaly on interdecadal time scale is more like a part of the meridional wave train originated from the northern Indian Ocean. The local cyclonic (high pressure) anomaly would favor the local ascending motion, leading to enhanced NECSR.

Note that, in the AGCM experiments, the idealized heating profile was prescribed with its maximum at 500 hPa over the northern tropical Atlantic (S1) and at 300 hPa over the Maritime Continent (S2). We have also calculated the observed diabatic heating profile over S1 and S2. The maximum diabatic heating over the warm SSTA region S1 appears around 500 hPa, and that of S2 appears between 400 and 200 hPa, which is approximately around 300 hPa (see Fig. S3 of the online supplemental material). A larger amplitude of diabatic heating in AGCM than the observed was prescribed so

as to obtain more robust atmospheric responses. We have rerun the ACGM with the observed heating profile, and the results remain qualitatively consistent.

This study has demonstrated the physical mechanisms of variabilities of the leading mode of NECSR during 1961–2012. Using the SSTA over the northern tropical Atlantic and Maritime Continent, the NECSR can be reconstructed to 32% and 50% of the total variances, respectively (see Fig. S5 of the online supplemental material). Therefore, seasonal prediction modeling can be conducted based on the SST indices over the two key regions if the SST has persistency. Besides, do the physical mechanisms involved in the precipitation variations also play a role in the temperature variations over NEC? Is there any seasonal dependency for the physical mechanisms responsible for rainfall variability over NEC? Does the mechanism of the interannual and interdecadal variabilities of NECSR still materialize at the intraseasonal time scale? These issues deserve further investigations.

Acknowledgments. The authors thank the three anonymous reviewers for their constructive comments. This work was supported by the National Key R&D Program of China (Grant 2018YFC1505905), the National Natural Science Foundation of China (Grants 41805048 and 41605035), the Liaoning Provincial Natural Science Foundation Project (the PhD Start-up Research Fund 2019-BS-214), and the Young Elite Scientists Sponsorship Program by CAST (2018QNRC001). This paper is ESMC Contribution Number 290.

REFERENCES

Bretherton, C. S., M. Widmann, V. P. Dymnikov, J. M. Wallace, and I. Blade, 1999: The effective number of spatial degrees of freedom of a time-varying field. *J. Climate*, **12**, 1990–2009, https://doi.org/10.1175/1520-0442(1999)012<1990:TENOSD>2.0.CO;2.

Chen, M., P. Xie, J. E. Janowiak, and P. A. Arkin, 2002: Global land precipitation: A 50-yr monthly analysis based on gauge observations. *J. Hydrometeor.*, **3**, 249–266, https://doi.org/10.1175/1525-7541(2002)003<0249:GLPAYM>2.0.CO;2.

Cui, Y. F., A. M. Duan, Y. M. Liu, and G. X. Wu, 2015: Interannual variability of the spring atmospheric heat source over the Tibetan Plateau forced by the North Atlantic SSTA. *Climate Dyn.*, **45**, 1617–1634, https://doi.org/10.1007/s00382-014-2417-9.

Du, H., Z. Wu, S. Zong, X. Meng, and L. Wang, 2013: Assessing the characteristics of extreme precipitation over northeast China using the multifractal detrended fluctuation analysis. *J. Geophys. Res. Atmos.*, **118**, 6165–6174, https://doi.org/10.1002/jgrd.50487.

Fang, Y., and Coauthors, 2018: The remote responses of early summer cold vortex precipitation in Northeastern China to the precedent sea surface temperatures. *Atmos. Res.*, **214**, 399–409, https://doi.org/10.1016/j.atmosres.2018.08.007.

Feng, X., X. Wang, and Y. Wang, 2006: Anomalies of the northeast China floods season precipitation and SVD analysis with SSTA in world oceans. *J. Trop. Meteor.*, **22**, 367–373, https://doi.org/10.16032/J.ISSN.1004-4965.2006.04.008.

Gao, J., and H. Gao, 2015: Relationship between summer precipitation over northeastern China and sea surface temperature in the southeastern Pacific and the possible underlying mechanisms (in Chinese). *Chin. J. Atmos. Sci.*, **39**, 967–977.

Gill, A. E., 1980: Some simple solutions for heat-induced tropical circulations. *Quart. J. Roy. Meteor. Soc.*, **106**, 447–462, https://doi.org/10.1002/qj.49710644905.

Giorgi, F., and Coauthors, 2012: RegCM4: Model description and preliminary tests over multiple CORDEX domains. *Climate Res.*, **52**, 7–29, https://doi.org/10.3354/cr01018.

Han, T., H. Chen, and H. Wang, 2015: Recent changes in summer precipitation in northeast China and the background circulation. *Int. J. Climatol.*, **35**, 4210–4219, https://doi.org/10.1002/joc.4280.

——, S. He, X. Hao, and H. Wang, 2018a: Recent interdecadal shift in the relationship between northeast China's winter precipitation and the North Atlantic and Indian Oceans. *Climate Dyn.*, **50**, 1413–1424, https://doi.org/10.1007/s00382-017-3694-x.

——, ——, H. Wang, and X. Hao, 2018b: Enhanced influence of early-spring tropical Indian Ocean SST on the following early-summer precipitation over northeast China. *Climate Dyn.*, **51**, 4065–4076, https://doi.org/10.1007/s00382-017-3669-y.

Held, I. M., and M. J. Suarez, 1994: A proposal for the intercomparison of the dynamical cores of atmospheric general circulation models. *Bull. Amer. Meteor. Soc.*, **75**, 1825–1830, https://doi.org/10.1175/1520-0477(1994)075<1825:APFTIO>2.0.CO;2.

Hu, K., R. Lu, and D. Wang, 2010: Seasonal climatology of cut-off lows and associated precipitation patterns over northeast China. *Meteor. Atmos. Phys.*, **106**, 37–48, https://doi.org/10.1007/s00703-009-0049-0.

Huang, B., and Coauthors, 2017: Extended Reconstructed Sea Surface Temperature, version 5 (ERSSTv5): Upgrades, validations, and intercomparisons. *J. Climate*, **30**, 8179–8205, https://doi.org/10.1175/JCLI-D-16-0836.1.

Jaiser, R., K. Dethloff, D. Handorf, A. Rinke, and J. Cohen, 2012: Impact of sea ice cover changes on the Northern Hemisphere atmospheric winter circulation. *Tellus*, **64A**, 11595, https://doi.org/10.3402/tellusa.v64i0.11595.

Kalnay, E., and Coauthors, 1996: The NCEP/NCAR 40-Year Reanalysis Project. *Bull. Amer. Meteor. Soc.*, **77**, 437–471, https://doi.org/10.1175/1520-0477(1996)077<0437:TNYRP>2.0.CO;2.

Li, F., and H. Wang, 2013: Autumn sea ice cover, winter Northern Hemisphere annular mode, and winter precipitation in Eurasia. *J. Climate*, **26**, 3968–3981, https://doi.org/10.1175/JCLI-D-12-00380.1.

Li, J., and B. Wang, 2018: Origins of the decadal predictability of East Asian land summer monsoon rainfall. *J. Climate*, **31**, 6229–6243, https://doi.org/10.1175/JCLI-D-17-0790.1.

Li, T., 2006: Origin of the summertime synoptic-scale wave train in the western North Pacific. *J. Atmos. Sci.*, **63**, 1093–1102, https://doi.org/10.1175/JAS3676.1.

Liu, Y., G. Huang, and R. Huang, 2011: Inter-decadal variability of summer rainfall in Eastern China detected by the Lepage test. *Theor. Appl. Climatol.*, **106**, 481–488, https://doi.org/10.1007/s00704-011-0442-8.

Lorenz, E. N., 1956: Empirical orthogonal functions and statistical weather prediction. MIT Department of Meteorology Statistical Forecast Project Tech. Rep. 1, 49 pp.

North, G. R., T. L. Bell, R. F. Cahalan, and F. J. Moeng, 1982: Sampling errors in the estimation of empirical orthogonal functions. *Mon. Wea. Rev.*, **110**, 699–706, https://doi.org/10.1175/1520-0493(1982)110<0699:SEITEO>2.0.CO;2.

Peng, S., and J. S. Whitaker, 1999: Mechanisms determining the atmospheric response to midlatitude SST anomalies.

J. Climate, **12**, 1393–1408, https://doi.org/10.1175/1520-0442(1999)012<1393:MDTART>2.0.CO;2.

Sardeshmukh, P. D., and B. J. Hoskins, 1988: The generation of global rotational flow by steady idealized tropical divergence. *J. Atmos. Sci.*, **45**, 1228–1251, https://doi.org/10.1175/1520-0469(1988)045<1228:TGOGRF>2.0.CO;2.

Shen, B., Z. Lin, R. Lu, and Y. Lian, 2011: Circulation anomalies associated with interannual variation of early-and late-summer precipitation in northeast China. *Sci. China Earth Sci.*, **54**, 1095–1104, https://doi.org/10.1007/s11430-011-4173-6.

Singarayer, J. S., J. L. Bamber, and P. J. Valdes, 2006: Twenty-first-century climate impacts from a declining Arctic sea ice cover. *J. Climate*, **19**, 1109–1125, https://doi.org/10.1175/JCLI3649.1.

Sun, B., and H. Wang, 2013: Water vapor transport paths and accumulation during widespread snowfall events in northeastern China. *J. Climate*, **26**, 4550–4566, https://doi.org/10.1175/JCLI-D-12-00300.1.

Sun, L., B. Shen, Z. Gao, B. Sui, L. Bai, S. Wang, G. An, and J. Li, 2007: The impacts of moisture transport of East Asian monsoon on summer precipitation in northeast China. *Adv. Atmos. Sci.*, **24**, 606–618, https://doi.org/10.1007/s00376-007-0606-8.

——, ——, B. Sui, and B. Huang, 2017: The influences of East Asian Monsoon on summer precipitation in northeast China. *Climate Dyn.*, **48**, 1647–1659, https://doi.org/10.1007/s00382-016-3165-9.

Takaya, K., and H. Nakamura, 2001: A formulation of a phase-independent wave-activity flux for stationary and migratory quasigeostrophic eddies on a zonally varying basic flow. *J. Atmos. Sci.*, **58**, 608–627, https://doi.org/10.1175/1520-0469(2001)058<0608:AFOAPI>2.0.CO;2.

Wang, H., and S. He, 2012: The increase of snowfall in northeast China after the mid-1980s. *Chin. Sci. Bull.*, **58**, 1350–1354, https://doi.org/10.1007/s11434-012-5508-1.

——, E. Yu, and S. Yang, 2011: An exceptionally heavy snowfall in northeast China: Large-scale circulation anomalies and hindcast of the NCAR WRF model. *Meteor. Atmos. Phys.*, **113**, 11–25, https://doi.org/10.1007/s00703-011-0147-7.

Wang, L., P. Xu, W. Chen, and Y. Liu, 2017: Interdecadal variations of the Silk Road pattern. *J. Climate*, **30**, 9915–9932, https://doi.org/10.1175/JCLI-D-17-0340.1.

Wu, B., R. Zhang, and D. Rosanne, 2008: Arctic dipole anomaly and summer rainfall in northeast China. *Chin. Sci. Bull.*, **53**, 2222, https://doi.org/10.1007/S11434-008-0229-1.

——, ——, and B. Wang, 2009: On the association between spring Arctic sea ice concentration and Chinese summer rainfall: A further study. *Adv. Atmos. Sci.*, **26**, 666–678, https://doi.org/10.1007/s00376-009-9009-3.

Wu, J., and X. Gao, 2013: A gridded daily observation dataset over China region and comparison with the other datasets. *Chin. J. Geophys.*, **56**, 1102–1111.

Zhao, J., J. Zhou, L. Yang, W. Huo, and G. Feng, 2018: Interannual and inter-decadal variability of early- and late-summer precipitation over northeast China and their background circulation. *Int. J. Climatol.*, **38**, 2880–2888, https://doi.org/10.1002/joc.5470.

Zhao, S., and J. Sun, 2007: Study on cut-off low-pressure systems with floods over northeast Asia. *Meteor. Atmos. Phys.*, **96**, 159–180, https://doi.org/10.1007/s00703-006-0226-3.

Zhou, B., Z. Wang, Y. Shi, Y. Xu, and Z. Han, 2018: Historical and future changes of snowfall events in China under a warming background. *J. Climate*, **31**, 5873–5889, https://doi.org/10.1175/JCLI-D-17-0428.1.

Zhu, C., L. Chen, and N. Yamazaki, 1999: The interdecadal variation characteristics of arctic sea ice cover-ENSO-East Asian monsoon and their interrelationship at quasi-four years time scale. *Adv. Atmos. Sci.*, **16**, 641–652, https://doi.org/10.1007/s00376-999-0038-8.

Zhu, Z., and T. Li, 2016: A new paradigm for continental U.S. summer rainfall variability: Asia–North America teleconnection. *J. Climate*, **29**, 7313–7327, https://doi.org/10.1175/JCLI-D-16-0137.1.

——, and ——, 2018: Amplified contiguous United States summer rainfall variability induced by East Asian monsoon interdecadal change. *Climate Dyn.*, **50**, 3523–3536, https://doi.org/10.1007/s00382-017-3821-8.

Supplemental Material

Supplementary information for *Journal of Climate* DOI:10.1175/JCLI-D-19-0302.1:

Interannual and interdecadal variabilities of spring rainfall over northeast China and their associated sea surface temperature anomalies forcings

Rui Lu, Zhiwei Zhu*, Tim Li and Haiyang Zhang

1, Key Laboratory of Meteorological Disaster, Ministry of Education (KLME)/Joint International Research Laboratory of Climate and Environment Change (ILCEC)/Collaborative Innovation Center on Forecast and Evaluation of Meteorological Disasters (CIC-FEMD), Nanjing University of Information Science and Technology, Nanjing, China

2, Yichun Meteorological Bureau, Heilongjiang Province, China

3, International Pacific Research Center and Department of Atmospheric Sciences, University of Hawaii at Manoa, Honolulu, Hawaii 96822

Corresponding author: Zhiwei Zhu, Nanjing University of Information Science and Technology, Ningliu Road 219, Meteorology Bldg. Jiangsu 210044, China. E-mail: zwz@nuist.edu.cn

This file includes:

Supplementary figures S1-S5

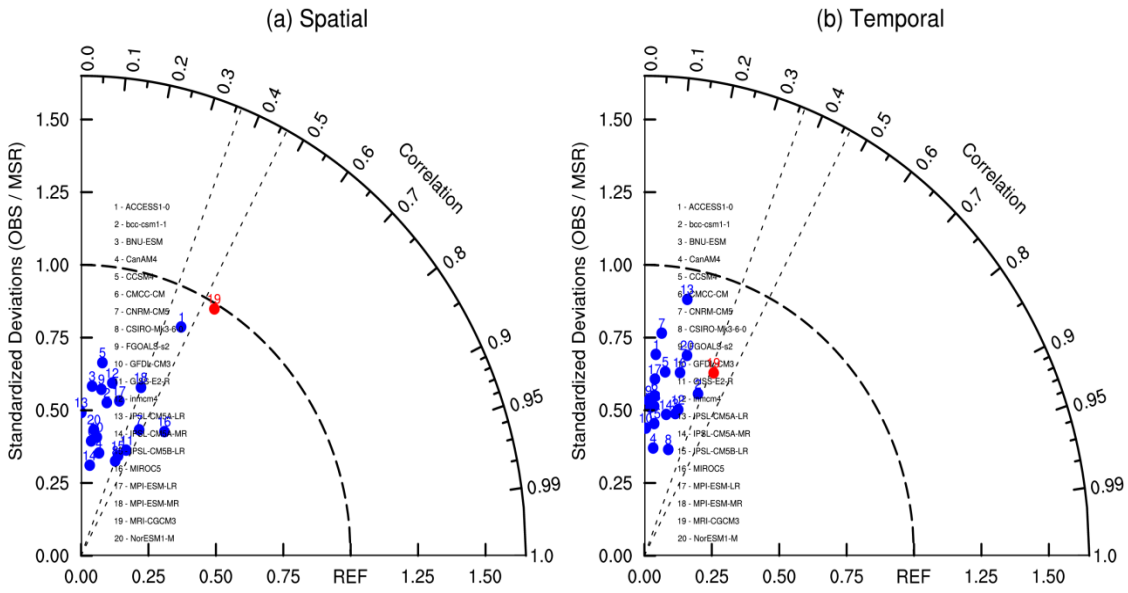

Fig. S1. Taylor diagrams of the (a) pattern (mm d^{-1}) and (b) principal component of the first EOF mode of NECSR (Northeast China Spring Rainfall) based on 20 AMIP (Atmospheric Model Intercomparison Project) models' outputs during 1979-2008 spring (March, April, May). The two dashed lines on the left (right) represent the 95% (99%) confidence level. The red dot represents the model that has highest skill in simulating the NECSR in terms of both the spatial and temporal distribution of the first EOF mode of NECSR.

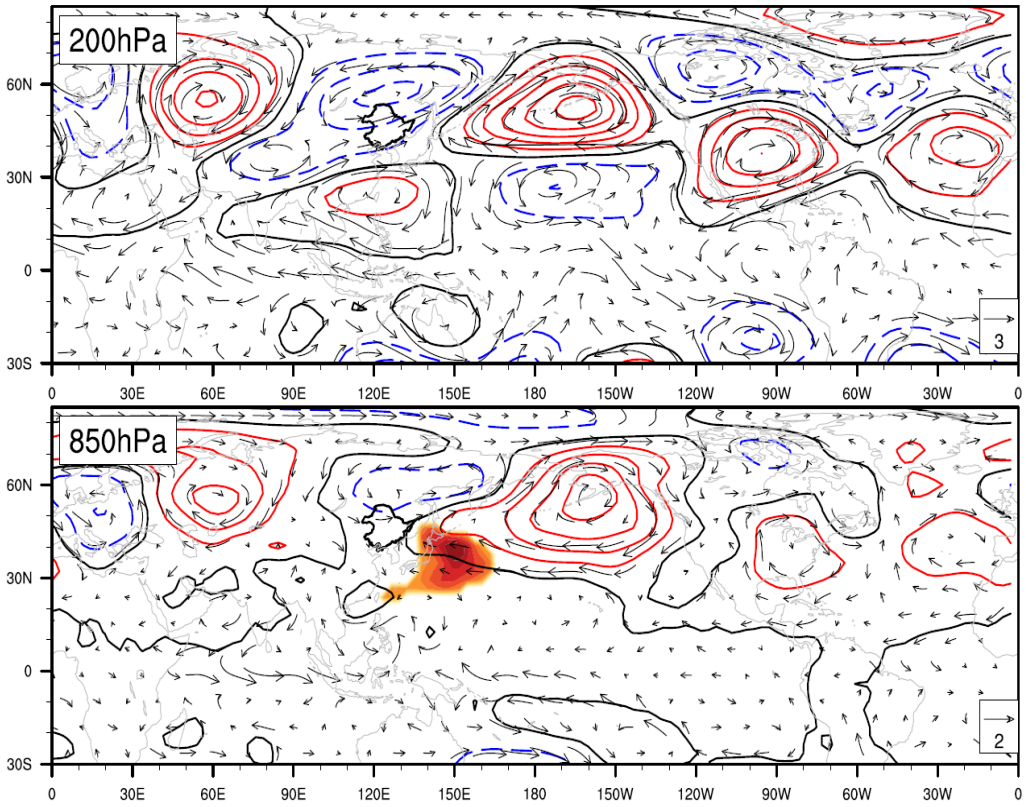

Fig. S2. The 200-hPa and 850-hPa geopotential height (contours; gpm) and wind (vectors; m s^{-1}) responses to the SSTA over the mid-latitude northwestern Pacific in ECHAMv4.6 (15-year integrated outputs of sensitivity experiment minus that of control experiment). The red shading indicates the additional SSTA over the mid-latitudes northwestern Pacific prescribed in the sensitivity experiment. The control experiment is run by using the climatological mean SST as the forcing. The black solid line delineates the region of NEC.

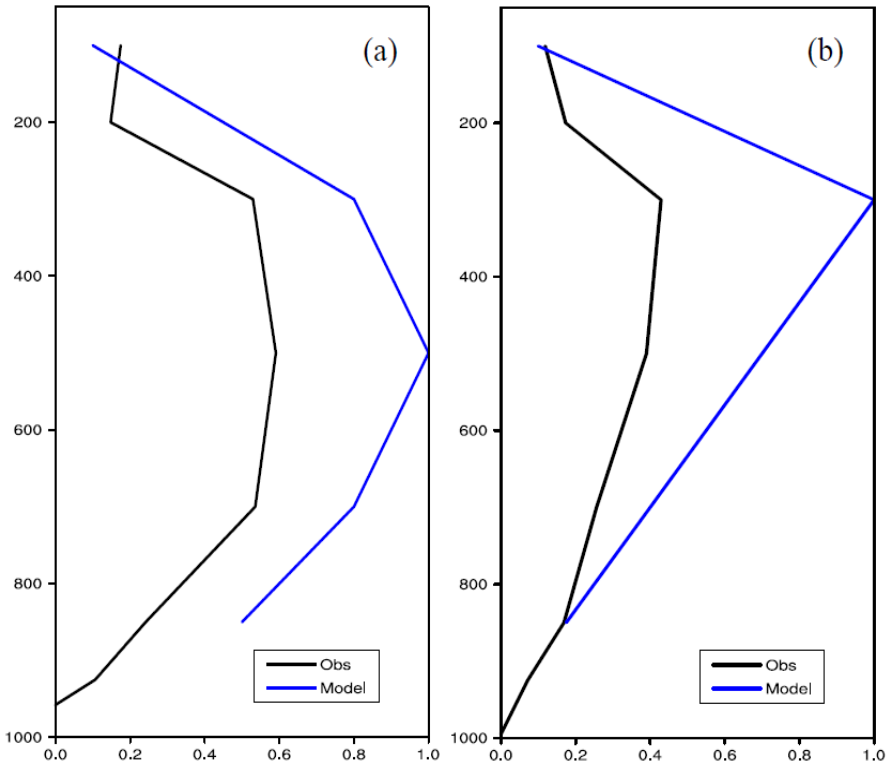

Fig. S3. The observed (black line; 1×10^{-1}K d^{-1}; derived from JRA-55 dataset) and the prescribed vertical profile of diabatic heating in the model (blue line; 1K d^{-1}) over (a) the northern equatorial Atlantic (S1 region), and over (b) the warm pool (S2 region).

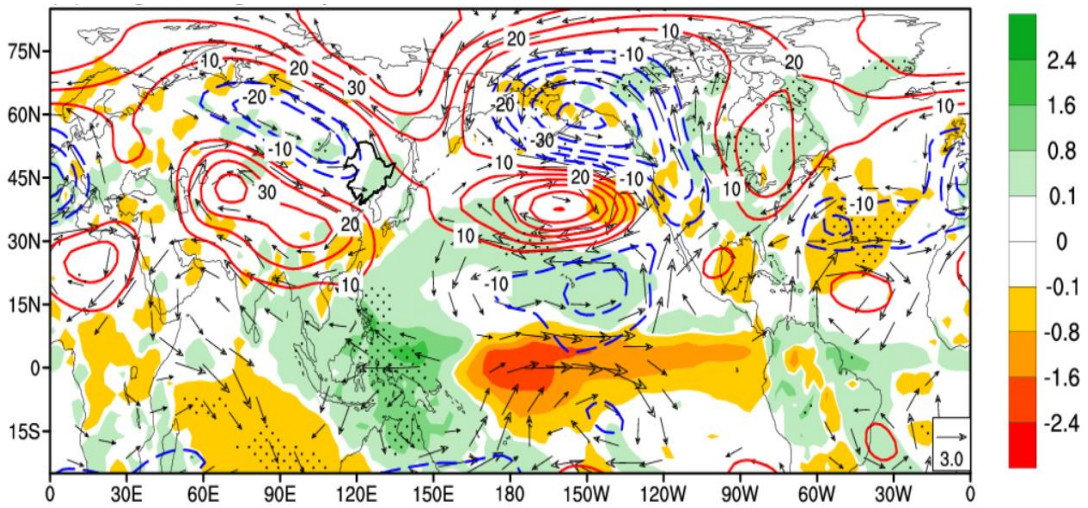

Fig. S4. Regressed 200-hPa geopotential height (contours; gpm), wind (vectors; m s^{-1}) and precipitation (shading; mm d^{-1}) in spring (MAM) onto the interdecadal component of PC1 after removing its linear trend.

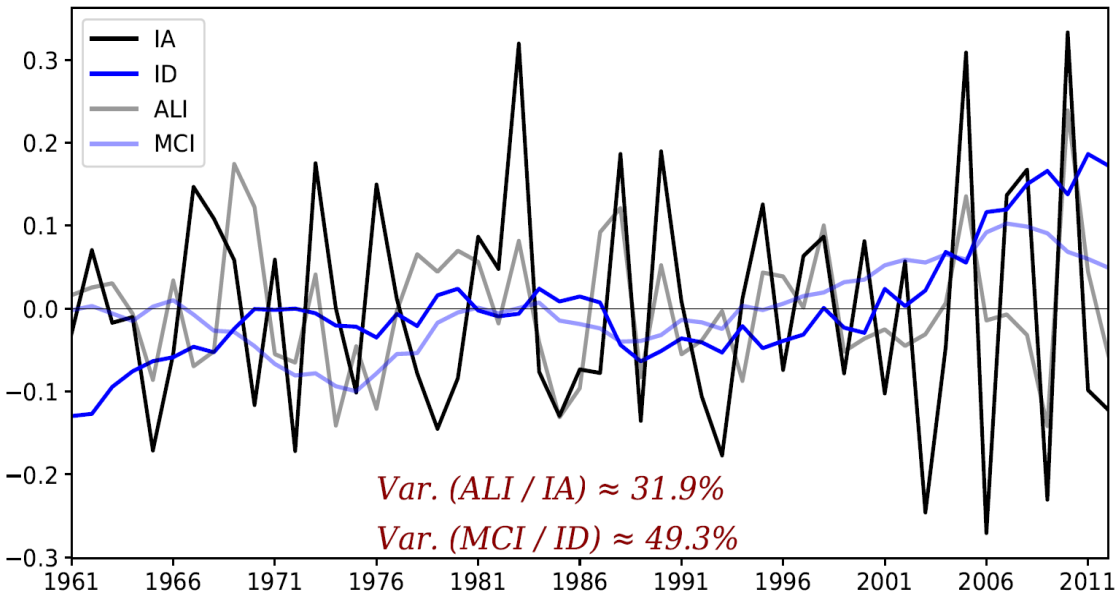

Fig. S5. The area-mean precipitation anomalies over NEC reconstructed by the interannual (black line) component of PC1, the interdecadal (blue line) component of PC1, the S1 SSTA (Atlantic SST Index, grey line) and the S2 SSTA (Maritime Continent SST Index, light blue line).